

1 **Electron flux models for different energies at**
2 **geostationary orbit**

R. J. Boynton,¹ M. A. Balikhin,¹ D. G. Sibeck,² S. N. Walker,¹ S. A.

Billings,¹ N. Ganushkina,^{3,4}

R. J. Boynton, Department of Automatic Control and Systems Engineering, University of Sheffield, Mapin Street, Sheffield S1 3JD, UK. (r.boynton@sheffield.ac.uk)

¹Department of Automatic Control and Systems Engineering, University of Sheffield, Sheffield S1 3JD, United Kingdom

²NASA Goddard Space Flight Center, Greenbelt, Maryland, USA

³Finnish Meteorological Institute, Helsinki, Finland

⁴University of Michigan, Ann Arbor, MI, USA

This is the author manuscript accepted for publication and has undergone full peer review but has not been through the copyediting, typesetting, pagination and proofreading process, which may lead to differences between this version and the Version of Record. Please cite this article

as doi:10.1002/2016SW001996 October 11, 2016, 7:55pm

D R A F T

3 **Abstract.** Forecast models were derived for energetic electrons at all en-
4 ergy ranges sampled by the third generation Geostationary Operational En-
5 vironmental Satellites (GOES). These models were based on Multi-Input Single-
6 Output (MISO) Nonlinear AutoRegressive Moving Average with eXogenous
7 inputs (NARMAX) methodologies. The model inputs include the solar wind
8 velocity, density and pressure, the fraction of time that the Interplanetary
9 Magnetic Field (IMF) was southward, the IMF contribution of a solar wind-
10 magnetosphere coupling function proposed by *Boynton et al.* [2011b] and the
11 Dst index. As such, this study has deduced five new 1-hour resolution mod-
12 els for the low energy electrons measured by GOES (30-50 keV, 50-100 keV,
13 100-200 keV, 200-350 keV and 350-600 keV) and extended the existing >800
14 keV and ≥ 2 MeV GEO electron fluxes models to forecast at a 1-hour res-
15 olution. All of these models were shown to provide accurate forecasts, with
16 prediction efficiencies ranging between 66.9% and 82.3%.

Author Manuscript

1. Introduction

17 The radiation belts consist of energetic particles trapped by the terrestrial magnetic
18 field and were discovered from the first in situ space radiation measurements. The outer
19 radiation belt is made up of trapped electrons ranging in energy from keVs to several
20 MeVs. *Blake et al.* [1992] and *Reeves* [1998] showed that the electron fluxes can vary by
21 several orders of magnitude in a few hours. The high fluence of these energetic electrons
22 can cause a number of problems on spacecraft depending on the electron energy. For
23 example, low energy electrons (1 keV to 100 keV) can cause surface charging that interferes
24 with the satellite electronic systems [*Olsen*, 1983; *Mullen et al.*, 1986], while higher energies
25 (above 1 MeV and above) cause deep dielectric charging that may permanently damage
26 the materials onboard the satellite [*Baker et al.*, 1987; *Wrenn et al.*, 2002; *Gubby and*
27 *Evans*, 2002; *Lohmeyer and Cahoy*, 2013; *Lohmeyer et al.*, 2015].

28 There are still many unanswered questions about the mechanisms involved within the
29 radiation belts, such as the acceleration mechanisms and loss processes of the electrons
30 [*Friedel et al.*, 2002]. Since we do not have a complete understanding of the physics,
31 radiation belt models based on first principals struggle to capture the variable dynamics
32 of the system [*Horne et al.*, 2013b]. As such, these models often exhibit large errors
33 between the forecast and the observed electron population [*Horne et al.*, 2013a].

34 The system identification approach has also been applied to modelling the radiation
35 belts. In this approach, models are automatically deduced from input-output data by the
36 system identification algorithms. The system identification methodologies include linear
37 prediction filters [*Baker et al.*, 1990], dynamic linear models [*Osthus et al.*, 2014], neural

38 networks [Koons and Gorney, 1991; Freeman et al., 1998; Ling et al., 2010], and Nonlinear
39 AutoRegressive Moving Average with eXogenous inputs (NARMAX) [Wei et al., 2011;
40 Boynton et al., 2013a, 2015]. While linear prediction filters and dynamic linear models
41 are suitable for linear systems, the main advantage of NARMAX and neural networks
42 is that they are capable of modelling nonlinear dynamics within the system. NARMAX
43 and neural networks can both provide accurate and reliable models for nonlinear systems
44 such as the radiation belts, however, NARMAX has the advantage of interpretability over
45 neural networks. Neural networks result in the relationship between input and output
46 measurements being described through a maze of multilayered neurones, in which each
47 connection has an associated weight factor and each neurone has an activation function.
48 This makes neural networks extremely difficult to interpret, i.e., to find out how the input
49 variables couple together to produce changes in the output. In contrast, NARMAX models
50 can result in a simple polynomial, from which understanding how the inputs change the
51 output is intuitive. Therefore, this study uses the NARMAX methodologies to model
52 the electron fluxes observed by the Geostationary Operational Environmental Satellites
53 (GOES), situated in Geostationary Earth Orbit (GEO).

54 The main aim of this study is to create reliable forecast models for the electron flux en-
55 ergy ranges observed by the third generation GOES. The second aim is to increase tempo-
56 ral resolution of the forecast to that which currently operates on the University of Sheffield
57 Space Weather Website (<http://www.ssg.group.shef.ac.uk/USSW/UOSSW.html>) and was
58 developed by Boynton et al. [2015]. In Section 2, we discuss the methodology used to de-
59 duce the forecast models. This includes a brief description of the NARMAX algorithm.
60 Section 3 presents an extension of the current 24-hour resolution > 800 keV and > 2

61 MeV GEO electron flux models, developed by *Boynton et al.* [2015], to 1-hour resolution
62 and a calculation of their performance. In Section 4, the methodology and data used
63 to derive the low energy models and the results of the models performances are shown.
64 The limitations of the models and their performance are discussed in Section 5 and the
65 conclusions from this study are presented in Section 6.

2. NARMAX Methodology

66 As stated in Section 1, NARMAX models provide reliable forecasts and are also easy to
67 interpret. As such, the methodology has been applied to a wide range of scientific fields,
68 from analysing the adaptive changes in the photoreceptors of *Drosophila* Flies [*Friederich*
69 *et al.*, 2009] to modelling the tide at the Venice Lagoon [*Wei and Billings*, 2006]. In the
70 field of space physics, the methodology was first used to model the Dst index using the half
71 wave rectifier (solar wind velocity multiplied by the southward IMF component) as the
72 input [*Balikhin et al.*, 2001; *Boaghe et al.*, 2001]. More recently, due to lack of knowledge
73 about the inputs to the Dst index system, *Boynton et al.* [2011b] used the NARMAX
74 model structure detection methodology to identify the main control parameter, or solar
75 wind coupling function, for geomagnetic storms quantified using the Dst index. This
76 coupling function was $p^{1/2}V^{4/3}B_T \sin^6(\theta/2)$, where p is the pressure, V is the velocity,
77 $B_T = \sqrt{B_y^2 + B_z^2}$ is the tangential IMF and $\theta = \tan^{-1}(B_y/B_z)$ is the clock angle of the
78 IMF in GSM co-ordinates). *Boynton et al.* [2011a] used this coupling function to deduce
79 a reliable model for the Dst index. *Boynton et al.* [2013b] and *Balikhin et al.* [2011]
80 employed a similar approach to identify the solar wind control parameters for electron
81 fluxes at GEO. In these studies, they found that the solar wind velocity and density
82 were the main control parameters. The interpretability of these results allowed *Balikhin*

83 *et al.* [2012] to make a direct comparison with the energy diffusion equation, where they
 84 found that acceleration due to local diffusion does not dominate at GEO. Recently, the
 85 NARMAX model structure detection methodology has been employed by *Beharrell and*
 86 *Honary* [2016] to determine the relationship between the solar wind and SYM-H.

87 NARMAX models were first proposed by *Leontaritis and Billings* [1985a, b] who demon-
 88 strated that the models have the potential to represent a wide class of nonlinear systems.
 89 A Multi-Input Single-Output (MISO) NARMAX model, which was used in this study to
 90 model the electron fluxes at GEO, is expressed by

$$\begin{aligned}
 y(t) = & F[y(t-1), \dots, y(t-n_y), \\
 & u_1(t-1), \dots, u_1(t-n_{u_1}), \dots, \\
 & u_m(t-1), \dots, u_m(t-n_{u_m}), \dots, \\
 & e(t-1), \dots, e(t-n_e)] + e(t)
 \end{aligned} \tag{1}$$

91 where y , u , and e represent the output, input and error terms respectively, $F[\cdot]$ repre-
 92 sents some nonlinear function (a polynomial in the case of this study), m is the number
 93 of system inputs and n_y , n_{u_1}, \dots, n_{u_m} , n_e are the maximum time lags for the output, each
 94 of the m inputs, and the error, respectively.

95 *Billings et al.* [1988] developed the first Forward Regression Orthogonal Least Squares
 96 (FROLS) algorithm that automatically fits a NARMAX model using input-output train-
 97 ing data sets. Simply put, the overall algorithm developed by *Billings et al.* [1988] involved
 98 three stages. The first stage is model structure detection, which identifies the variables
 99 or combination of variables that control the evolution of the system. In Equation 1, the
 100 expansion of $F[\cdot]$ in terms of a high degree polynomial, results in a huge number of mono-

101 mials, especially if there are many possible inputs. The vast majority of the possible
102 monomials will have little influence on the system, i.e., the coefficients of the monomial
103 will be zero. Therefore, only a small number of monomials are required to represent the
104 dynamics of the system. The FROLS procedure identifies the most significant monomi-
105 als by use of the Error Reduction Ratio (ERR). Once the model structure is detected,
106 the second stage is to estimate the coefficient for each of the monomials detected in the
107 model. These first two stages are referred to as training the model. The final stage is to
108 validate the model. Since its inception, many variants on the FROLS algorithm have been
109 developed [*Billings et al.*, 1989; *Mao and Billings*, 1997; *Wei and Billings*, 2008]. This
110 study employs the Iterative Orthogonal Forward Regression (IOFR) algorithm, developed
111 by *Guo et al.* [2014], which is more likely to detect the optimal model when the data is
112 oversampled.

113 The IOFR is largely based upon the initial FROLS algorithm, where the ERR of each
114 of the monomials is calculated with respect to the output. The monomial with the highest
115 ERR is then selected as the first monomial for the initial model structure. For the next
116 step of the algorithm, all other monomials are orthogonalized relative to the first monomial
117 that has just been selected. This effectively removes the first monomials contribution to
118 the output from the remaining monomials. The ERR of these orthogonalized monomials
119 are then calculated with respect to the output and the one with the highest ERR is
120 selected as the second monomial for the initial model. For the third step, the remaining
121 monomials are orthogonalised relative to both the first and second monomials selected
122 for the initial model and the ERR is calculated. Again, the orthogonalised monomial
123 with the highest ERR is selected and this will be the third monomial for the model. This

124 process of orthogonalizing the remaining monomials with respect to all the selected model
 125 terms then selecting the orthogonalised monomial with the highest ERR for the model is
 126 continued until the model has the optimum number of model monomials. To decide the
 127 optimum number of model terms, this study employed the Adjustable Prediction Error
 128 Sum of Squares (APRESS) [Billings and Wei, 2008]. After each monomial is selected
 129 during every step of the FROLS algorithm, the APRESS is calculated from the ERR

$$APRESS = \frac{1}{(1 - \lambda k/N)^2} \left(1 - \sum_{i=1}^k ERR_i \right) \quad (2)$$

130 where N is the number of data points, k is the number of monomials that have been
 131 selected and λ is an adjustable factor that was between 5 and 10. At each step, i ,
 132 $APRESS(i)$ is calculated and compared to the previous $APRESS(i - 1)$. APRESS
 133 will decrease as each significant monomial is added to the model until a local minima is
 134 reached. After this turning point, the addition of more model monomials is less likely
 135 to increase the performance of the model and may lead to the model becoming overfit
 136 [Billings and Wei, 2008]. Therefore, the turning point in APRESS dictates the optimum
 137 number of model monomials and the initial model polynomial structure is obtained. A
 138 least squares procedure then identifies the coefficients for each monomial to yield the
 139 model.

3. Increasing the time resolution of the existing > 800 keV and > 2 MeV GEO electron flux models

140 Models for forecasting the fluxes of > 800 keV and > 2 MeV electrons at GEO were
 141 developed by Boynton et al. [2015]. These models were deduced using the NARMAX
 142 methodology and provide a 1-day resolution forecast for one day ahead. Both of these
 143 models were shown to have a high prediction efficiency for estimating the next day's

144 electron flux value [Boynton *et al.*, 2015]. The forecast results can be found online at
145 www.ssg.group.shef.ac.uk/USSW/UOSSW.html.

146 The original model only produces one forecast for the day. This forecast is for the
147 average electron flux between 00:01 UTC one day to 00:00 UTC on the next day, calculated
148 at 00:01 UTC. This means at the start of every UTC day the original model calculates a
149 forecast for the average electron flux over the next 24 hour. One of the aims of this study
150 is to increase the temporal resolution of these forecasts. Therefore, the time resolution of
151 the > 800 keV and > 2 MeV GEO electron flux models were extended to give a forecast of
152 the electron fluxes every hour for the next 24 hours in contrast to only one daily forecast
153 per day. This means that every hour the model will calculate a forecast for the average
154 electron flux over the next 24 hour, producing 24 forecasts per day.

3.1. Data and methodology

155 The > 800 keV and > 2 MeV electron flux models rely on solar wind inputs to forecast
156 the electron flux. The solar wind inputs are the daily average velocity and density; and
157 the amount of time the IMF is southward in a 24 hour period. The 1-minute solar wind
158 velocity, density and IMF B_z -component data were obtained from the OMNI website
159 (http://omniweb.gsfc.nasa.gov/ow_min.html) from 1 January 2011 to 28 February 2015.
160 At every hour, the past 24 hour average of the solar wind velocity and density was cal-
161 culated. For example, the point at 10:00:00 UTC on 5 January 2015 is an average of the
162 1440 1-minute points between 10:01:00 UTC on 4 January 2015 and 10:00:00 UTC on 5
163 January 2015. In addition, the number of minutes that the IMF was southward during
164 the past 24 hours was determined for the final input.

165 The electron flux data used to analyse the performance of the extended temporal res-
166 olution > 800 keV and > 2 MeV GEO electron flux models were from GOES 13. The
167 electron fluxes onboard the GOES 13 satellite are measured by the Energetic Proton Elec-
168 tron and Alpha Detector (EPEAD) [Hanser, 2011] and the MAGnetospheric Electron De-
169 tector (MAGED). [Hanser, 2011]. The data for these instruments can be accessed from
170 <http://www.ngdc.noaa.gov/stp/satellite/goes/dataaccess.html> and the MAGED will be
171 discussed in Section 4.1.

172 The EPEAD measures the relativistic integral electron fluxes and has two detectors
173 pointing in opposite directions, both tangential to the spacecrafts orbit, named the east
174 and west detectors. Since the EPEAD measures integral flux, the > 2 MeV electrons
175 will be measured by the > 800 keV channel, however, the > 2 MeV electrons account for
176 less than 1% of the electrons detected on average. These data were used to assess the
177 1-hour temporal resolution of the SNB³GEO electron flux models (SN stands for Sheffield
178 NARMA, B³ corresponds to the letters of surnames of three model developers and GEO
179 stands for geostationary orbit). The data period used for this part of the study was from
180 1 January 2011 to 28 February 2015. The study employed the > 800 keV and > 2 MeV
181 energy channels from both the east and west detectors onboard the GOES 13 satellite.
182 The 5-minute proton corrected electron flux values were averaged between the east and
183 west detectors. This was then time averaged resulting in a data set with 1-hour resolution,
184 such that each 1-hour point was determined by averaging the 5-minute data over the past
185 24 hours, e.g., the point at 10:00:00 UTC on 5 January 2015 is average of the 288 5-minute
186 points between 10:05:00 UTC on 4 January 2015 and 10:00:00 UTC on 5 January 2015.
187 This data was then compared to the model forecast. The one hour moving average

188 data will allow for a more continuous forecast of the daily average electron flux, such that
 189 every hour the online model will be able to forecast the electron flux value over the next
 190 24 hours, compared to only producing one forecast for each UTC day. Therefore, the
 191 forecast horizon for both the >800 keV and >2 MeV models will be 24 hours.

3.2. Model Performance

192 The > 800 keV and > 2 MeV GEO electron flux models were run using the 1-hour
 193 resolution input data and the results were compared to the EPEAD 1-hour electron flux
 194 data, for the period from 1 January 2011 to 28 February 2015. The performance of the
 195 models during the period could then be analysed.

The performance of the models was assessed statistically by the Correlation Coefficient (CC), Eq. (3) and the Prediction Efficiency (PE), Eq. (4), which are commonly used to assess models [Temerin and Li, 2006; Li, 2004; Boynton et al., 2011a; Wei et al., 2004; Boynton et al., 2015; Rastatter et al., 2013].

$$\rho_{y\hat{y}} = \frac{\sum_{t=1}^N [(y(t) - \bar{y})(\hat{y}(t) - \bar{\hat{y}})]}{\sqrt{\sum_{t=1}^N [(y(t) - \bar{y})^2] \sum_{t=1}^N [(\hat{y}(t) - \bar{\hat{y}})^2]}} 100\% \quad (3)$$

$$E_{PE} = \left[1 - \frac{\sum_{t=1}^N [(y(t) - \hat{y}(t))^2]}{\sum_{t=1}^N [(y(t) - \bar{y})^2]} \right] 100\% \quad (4)$$

196 Here, E_{PE} is the PE, ρ is the CC, $y(t)$ is the output at time t , \hat{y} is the estimated output
 197 from the model, N is the length of the data and the bar signifies the average.

3.2.1. > 800 keV model

199 Panel (a) of Figure 1 shows the past 24 hour average > 800 keV electron flux measured
200 by GOES in blue and the model 24 hour ahead forecast in orange for the period from 1
201 January 2011 to 28 February 2015, while below in panel (b) of Figure 1 depicts the model
202 error ($e = \log_{10}(J_{GOES}) - \log_{10}(J_{model})$). During this period, the PE was 72.1% and the
203 CC was 91.1%

204 3.2.2. > 2 MeV model

205 Panel (c) of Figure 1 shows the past 24 hour average > 2 MeV electron flux measured
206 by GOES in blue and the model 24 hour ahead forecast in orange for the period from
207 1 January 2011 to 28 February 2015, while below in panel (d) of Figure 1 depicts the
208 > 2 MeV electron flux model error. The PE for the > 2 MeV model was 82.3% while
209 the CC was 90.9%. Figures 1 (a) and (c) reflect the better statistical performance of the
210 > 2 MeV model over the > 800 keV model, since it can clearly be seen that the > 2
211 MeV model follows more closely the blue observed GOES electron flux, particularly for
212 the lower electron flux values.

4. Modelling the low energy electron fluxes measured by GOES 13

213 Models to forecast the low energy electrons measured by GOES satellites were deduced
214 using the NARMAX IOFR algorithm. This method requires input-output data for train-
215 ing the models.

4.1. Data and Methodology

216 The electron flux data for the training and validation of these models comes again from
217 GOES 13. The MAGED has 9 telescopes pointing in different directions and measures
218 the lower energy differential electron fluxes in 5 energy channels: 30-50 keV, 50-100 keV,

219 100-200 keV, 200-350 keV and 350-600 keV [Hanser, 2011]. The data period used for this
220 part of the study was from 1 May 2010 to 28 February 2015 and employed all energy
221 channels available from the instrument. This study is concerned mainly with the trapped
222 electrons and therefore should not use a telescope that is directed in the loss cone, which
223 is $< 5^\circ$ \rightarrow CED. Since telescopes 1-5 of the MAGED are in the east-west plane, they
224 should be directed further away from the loss cone than telescopes 6-9, which are directed
225 north or south. Figure 2(a) show the 30-50 keV electron flux for the 9 telescopes and
226 Figure 2(b) shows the pitch angle for each of the telescopes, which can be downloaded
227 from <http://www.ngdc.noaa.gov/stp/satellite/goes/dataaccess.html>. These are displayed
228 for an arbitrary period between 13 November 2012 and 27 October 2013. The Figure
229 shows that telescopes 1-6 have pitch angles between $\sim 110^\circ$ and $\sim 40^\circ$ degrees and with a
230 telescope cone angle of 30° none of these should be directed in the loss cone. Since GOES
231 13 is positioned above the equator at $\sim 0^\circ$ latitude and the magnetic north pole is $\sim 60^\circ$
232 West of the satellite and has a latitude of $\sim 85^\circ$ North during this period, the telescope
233 pointing furthest south (telescope 7) is the only one permanently looking in the loss cone.
234 As such, the electron flux of telescope 7 is less than the others. Therefore, we arbitrarily
235 chose the data from telescope 3 to use as the output for this particular study. Using only
236 one telescope makes the real-time online procedure of processing the data more simple,
237 which will reduce the possibility of bugs occurring thus making the real time procedure
238 more reliable.

239 Solar wind and geomagnetic indices were used as input data for training the mod-
240 els. The 1-minute solar wind velocity, density and IMF data were obtained from the
241 OMNI website (http://omniweb.gsfc.nasa.gov/ow_min.html), while the Dst geomagnetic

242 index was from the World Data Center for Geomagnetism, Kyoto ([http://wdc.kugi.kyoto-](http://wdc.kugi.kyoto-u.ac.jp/index.html)
243 [u.ac.jp/index.html](http://wdc.kugi.kyoto-u.ac.jp/index.html)).

4.2. Model Training

244 The training data was from 1 March 2011 to 28 February 2013. For the training data,
245 the 1-minute corrected electron flux values were daily averaged between 00:01:00 UTC
246 and 00:00:00 UTC the next day for each day, resulting in training 790 data points. This
247 was chosen because a NARMAX model requires a training set that covers a wide range of
248 the system's variation, which is usually approximately a few hundred data points *Billings*
249 *et al.* [1987].

250 The studies by *Boynton et al.* [2013b] and *Balikhin et al.* [2012] showed that the time
251 delay in the reaction of electron fluxes to changes in the solar wind increase with the
252 energy. The high energy models of > 800 keV and > 2 MeV had minimum time delays
253 of one day and thus it is possible to forecast one day into the future. However, same day
254 values of the solar wind affect the current low energy electron flux. Therefore, it is not
255 possible to forecast one day ahead. To get around this problem, the past 24 hour averages
256 were calculated for each hour, as previously described. Therefore, the input time lags in
257 the algorithm, n_{um} , were shifted hourly not daily. For example, if input $U(t - 10$ hours)
258 is selected by the model, this monomial represents the average of the points between
259 $U(t - 10$ hours) and $U(t - 34$ hours). Initially, a number of window intervals from 1
260 hour averages, past 3 hours, past 12 hours as well as 24 hours were investigated. The 12
261 and 24 hour windows gave the better results but it was decided to use 24 hour averaging
262 for convenience because the same inputs could be used for > 2 MeV and 800 keV models.

263 This also makes the procedure simpler when implemented online and therefore less chance
264 of bugs.

265 The algorithm was run for the 5 energy ranges using lagged inputs from 2 to 48 hours.
266 These inputs were the solar wind velocity V and density n , the amount of time the
267 IMF is southward in a 24 hour period T_{Bs} , the Dst index, and the term resulting
268 from the coupling function proposed by *Balikhin et al.* [2010] and *Boynton et al.* [2011b],
269 $B_T \sin^6(\theta/2)$ (where $B_T = \sqrt{(B_y^2 + B_z^2)}$ is the tangential IMF and $\theta = \tan^{-1}(B_y/B_z)$ is
270 the clock angle of the IMF). Therefore, the NARXAX model of the electron flux J will
271 be

$$\begin{aligned}
 J(t) = & F[J(t-24), J(t-48), \\
 & V(t-2), V(t-3), \dots, V(t-48), \\
 & n(t-2), n(t-3), \dots, n(t-48), \\
 & T_{Bs}(t-2), T_{Bs}(t-3), \dots, T_{Bs}(t-48), \\
 & Dst(t-2), Dst(t-3), \dots, Dst(t-48), \dots, \\
 & B_T \sin^6(\theta/2)(t-2), B_T \sin^6(\theta/2)(t-3), \dots, B_T \sin^6(\theta/2)(t-48), \\
 & e(t-24), e(t-48)] + e(t)
 \end{aligned} \tag{5}$$

272 where the lags are in hours. When F is expanded to a second degree polynomial, there
273 will be over 10 thousand monomials for the FROLS algorithm to search through.

274 For the 30-50 keV electrons, a compromise had to be made between producing a reliable
275 forecast and the forecast horizon, the amount of time the model can forecast into the
276 future. The model detected by the algorithm included input terms, I , with a minimum
277 lag of 6 hours $J(t) = F[I(t-6), \dots]$. Therefore, employing the inputs at the present time t ,

278 it is possible to estimate the electron flux 6 hours into the future, $J(t+6) = F[I(t), \dots]$. To
 279 increase the forecast horizon, the ≤ 6 hour time lagged monomials were manually removed
 280 from the algorithms search to see if the performance of the model, based on PE and the
 281 CC, dropped significantly on a period of test data from 1 May 2010 to 28 February 2011. It
 282 was found there was only a negligible drop in performance if the detected model had input
 283 terms with a minimum of 7 hour time lag. This process of manually removing monomials
 284 with larger and larger time lags was continued until there was a significant performance
 285 drop in the model output. Figure 3 shows the results of this process with PE having a
 286 significant drop at a minimum lag of 11 hours. Therefore, the model with a minimum of
 287 10 hours lag was selected as the final 30-50 keV model and could forecast the past 24 hour
 288 average of the flux 10 hours in the future. This methodology was repeated for the other
 289 4 energy channels and as with the studies by *Boynton et al.* [2013b] and *Balikhin et al.*
 290 [2012], the time delay of electron fluxes increased with the energy. The forecast horizons
 291 for each of the models is shown in Table 1. In each of the NARMAX models, the monomial
 292 with the minimum lag is due to a velocity component within the monomial. For example,
 293 in the 30-50 keV model, the FROLS algorithm selected $V(t-10)B_T \sin(\theta/2)(t-12)$ as the
 294 exogenous monomial with the highest ERR. The exogenous monomial with the highest
 295 ERR in each of the models had a component of the velocity at the models minimum lag.
 296 For the three lowest energies the velocity was coupled with the IMF factor, while for the
 297 two higher energies the FROLS algorithm selected the linear velocity.

4.3. Final Model Performance

298 The performance of the models were analysed statistically using the PE and CC. Each
 299 of the models were run on the data from 1 March 2013 to 28 February 2015. At first, the

300 models were run on the daily averaged data which resulted in 730 points for the period.
301 Then, the models were extended to 1-hour resolution of the past 24 hour average, which
302 contains 17520 points, to assess each of the models performance with an increased time
303 resolution.

304 Table 1 lists the performance of the five low energy electron flux models, showing the
305 PE and CC for the 1-day and 1-hour resolution data. The Table also shows the minimum
306 time lag used in the model and thus how far ahead the model can forecast into the future.
307 This is in agreement with the studies by *Boynton et al.* [2013b] and *Balikhin et al.* [2012],
308 since the minimum time lags increase with energy. The PE of the models are between
309 66.9% and 73.6%, which means that the mean square error is well within the variance
310 of the fluxes, and the CC 82% and 85.9%. The results of the five models for the 1-hour
311 resolution data are illustrated in Figures 4 (a) (30-50 keV model), 4 (c) (50-75 keV model),
312 4 (e) (100-200 keV model), 5 (a) (200-350 keV model) and 5 (c) (350-600 keV model).
313 These figures show the observed GOES electron flux in blue and the model forecast in
314 orange. Below each of these figures are their respective model error plots in blue, where
315 the dashed black line is zero error. The figures show that the models approximately
316 follow the measured fluxes with the errors within one order of magnitude.

5. Discussion

317 One of the aims of this study was to increase the time resolution of the forecasts of the
318 > 800 keV and > 2 MeV GEO electron fluxes models that currently operate online. These
319 models provide daily averaged one day ahead forecasts for each UTC day. Increasing the
320 resolution of the model by using one hour averages of the GOES data is not that simple
321 because during a 24 hour GEO orbit there is a significant spatial variation of the electron

322 fluxes that is independent of any temporal changes due to adiabatic acceleration and
323 loss. This is due to changes in the structure of the terrestrial magnetic field, where the
324 compressed dayside leads to an increase in the strength of the magnetic field compared to
325 the nightside. As electrons drift from the nightside to the dayside, these changes in the
326 structure of the magnetic field cause the electrons to move outward as they approach noon
327 and back inward as they drift back to midnight. Since the electron flux is generally greater
328 deeper within the magnetosphere, higher fluxes are observed when GOES is situated at
329 noon compared to midnight. This spatial variation makes it difficult to deduce a data
330 based model because the satellites position is always changing. As such, to achieve the
331 aim of increasing the temporal resolution, we employed a moving average of the preceding
332 24 hours calculated every hour. We applied the existing > 800 keV and > 2 MeV GEO
333 electron flux models to this 1-hour averaged data because these models have already been
334 proven to be reliable in their online operation [Balikhin *et al.*, 2016]. This change in input
335 time resolution resulted in high values for the PE and CC, higher than those reported by
336 Boynton *et al.* [2015]. Boynton *et al.* [2015] showed, using the 1-day resolution data, that
337 the > 2 MeV model had a PE of 78.6% and a CC of 89.4% and that the > 800 keV model
338 had a PE of 70% and a CC of 84.7% between the 1 January 2011 and 30 June 2012, all
339 of which are lower than the results shown in this study. However, these statistics should
340 really be compared over the same time time period. Based on the time period between the
341 1 January 2011 and 30 June 2012 the 1 hour PE was 76.0% and the CC was 87.5% for the
342 > 800 keV model and the PE was 82.3% and the CC was 90.8% for the > 2 MeV model.
343 Therefore, these models perform better using the 1-hour resolution data. It can be seen
344 that the >2 MeV model has a higher PE and CC than the >800 keV model for all the

345 periods of data. One of the explanations for this could be that since it takes more time
346 for the electrons to be accelerated to >2 MeV, this larger time delay may allow for a more
347 accurate prediction. Another explanation is that the variance of the GOES logarithmic
348 >2 MeV fluxes was over twice that of the logarithmic > 800 keV fluxes for this time period
349 and since prediction efficiency is dependent on the variance of the observed signal, a larger
350 variance for the same mean squared error will mean a higher prediction efficiency. Three
351 out of the five lower energy models also performed better using the 1-hour resolution data,
352 where only the two lowest energy models had lower performance statistics on the 1-hour
353 resolution data compared to the 1-day resolution data.

354 One of the limitations of the three lowest energy electron models is that the advance
355 time of the forecast is less than the higher energy models, since the low energy electron
356 fluxes at GEO respond to solar wind changes significantly faster than high energy electrons
357 [*Balikhin et al.*, 2012; *Boynnton et al.*, 2013b]. The 30-50 keV model is only able to forecast
358 the 24 hour average electron flux 10 hours into the future, which means that 14 hours
359 of this average is already measured. Also, it should be noted that better models with
360 higher performance statistics for the MAGED models, except for the 350-600 keV energy
361 channel, could be obtained if the forecast length was sacrificed. For example, the 30-50
362 keV model had a 4% higher PE if 6 hour time lags were included in the algorithm but
363 this would mean that 18 hours of the forecast had already been measured by GOES.

364 The distributions of the model errors ($\log_{10}(J_{GOES}) - \log_{10}(J_{model})$) were plotted to
365 provide some technical information about the quality of the models. Moreover, the dis-
366 tribution of model errors when the Dst index <-40 nT were also plotted to show the
367 models performance during geomagnetic activity. Figure 6 shows the distributions for the

368 MAGED energies, while Figure 7 shows the distributions for the EPS energies. The vari-
369 ance of the model errors, σ_e , is also shown in the top right distributions. The distribution
370 of the model errors for all energies resemble a normal distribution. For the EPS energy
371 models, the distribution of the errors is wider, which could be due to the larger variance
372 of the integral fluxes. From the channels between 200-350 keV to > 2 MeV (Figures 6
373 (g), 6 (i), 7 (a) and 7 (c)), it can be seen that more errors occur < -0.5 than > 0.5 . The
374 errors < -0.5 indicate that the model prediction was higher than the GOES observation.
375 This could be due to the model overshooting or missing electron flux dropouts. When
376 inspecting the model error distribution during geomagnetically active times, the trend of
377 more negative errors occurring can be seen down to the 100-200 keV (Figures 6 (f), 6 (h),
378 6 (j), 7 (b) and 7 (d)). This implies that these models tend to overshoot or miss dropouts
379 during geomagnetic storms.

380 To investigate whether the model is tending to overshoot or miss dropouts, the model
381 output vs observed values were plotted for 1 month time scales along with the Dst index.
382 Figure 8 shows the observed electron flux in blue with the model forecast in orange for the
383 various energy channels in panels (a)-(g) and the Dst index in panel (h) between 15 April
384 2013 and 15 May 2013. The figure shows that a moderate geomagnetic storm occurs on the
385 24 of April with a Dst index of ~ -50 nT, which results in the enhancement of the electron
386 fluxes for all energy ranges, with the lower energies reacting on the same day as the main
387 phase of the storm and the highest energies peaking a couple of days after, during the
388 storm recovery. This enhancement of the fluxes is forecast by each of the models, with all
389 models increasing within a few hours of the actual onset, some models a few hours before
390 (>2 MeV) and others a few hours after (350-600 keV). Another moderate storm occurs on

391 1 May 2016 with a Dst index of ~ -65 nT. This storm causes a dropout of electron fluxes
392 that recovers the next day for energies >100 keV, while causing an enhancement in the
393 two lowest energy channels. The two models for the two lowest energy channels manage to
394 forecast the fluxes accurately, however, the 5 models that predict fluxes >100 keV do not
395 manage to forecast the dropout. Another dropout occurs on 4 May 2013, during a small
396 storm, for energies >100 keV, while the lower energies had slower decay starting at the
397 same time as the recovery phase of the previous storm on 1 May 2013. Again, the model
398 forecast misses the dropout and so the model error ($e = \log_{10}(J_{GOES}) - \log_{10}(J_{model})$) is
399 negative. This trend is prevalent throughout the data and helps to explain why more
400 large negative errors occur in the distribution figures (6 and 7). One of the reasons why
401 the models miss the dropouts in electron fluxes could be due to a faster time scale for
402 the dropouts. The models with energies > 100 keV have minimum lags ≥ 16 hours. If
403 the time scales of the dropouts occur quicker than this then the model will not be able to
404 forecast the dropouts.

405 If the models fail to predict a dropout or an enhancement, the models tend to lag the
406 output by 24 hours. This is due to the past value of electron flux term, $J(t - 24)$, within
407 the models. For example, in the case of a missed dropout, the model output will continue
408 as if the sudden change in electron flux has not occurred until after 24 hours when the
409 change in the $J(t - 24)$ monomial, due to the dropout 24 hours earlier, causes the model
410 to decrease. This results in the 24 hour delay that can occur with the models.

411 It is worth noting that the convective and substorm-associated electric fields strongly
412 affect the evolution of keV electron fluxes within the inner magnetosphere [*Ganushkina*
413 *et al.*, 2013, 2014, 2015], leading to flux variations on time scales significantly shorter

414 then 24 hours. The Inner Magnetosphere Particle Transport and Acceleration Model
415 (IMPTAM) can provide a good nowcast of the short time scale variations, but the model
416 is not able to forecast in advance [*Ganushkina et al.*, 2015].

417 There are other applications of the models in addition to providing forecasts of the
418 electron fluxes. The models could potentially be employed for the prediction of wave
419 intensities. This could be achieved by using the NARMAX electron flux models in combi-
420 nation with models deduced by *Li et al.* [2013] or *Mourenas et al.* [2014], which are able
421 to estimate the wave activity from the dynamics of electron fluxes.

6. Conclusions

422 The aim of this study was to create forecast models for the electron flux energy ranges
423 observed by the third generation GOES satellites, which have an increased temporal
424 resolution over the > 800 keV and > 2 MeV GEO electron fluxes models that were
425 previously developed *Boynton et al.* [2015]. The increase in time resolution provided by
426 the one hour moving average data allow for a more continuous forecast of the daily average
427 electron flux rather than producing only one forecast for each UTC day. Instead, every
428 hour the online model is able to forecast the electron flux value over the next 24 hours.
429 As such, this study has deduced five new 1-hour resolution models for the low energy
430 electrons measured by GOES, ranging in energy from 30 keV to 600 keV and extended
431 the existing > 800 keV and > 2 MeV GEO electron fluxes models to forecast at a 1-hour
432 resolution. These models had prediction efficiencies between 66.9% and 73.6% for the
433 period between 1 March 2013 and 28 February 2015.

434 All of these models are implemented in real time to forecast the electron fluxes
435 at GEO and can be found at the University of Sheffield Space Weather website
436 (www.ssg.group.shef.ac.uk/USSW2/UOSSW.html).

437 **Acknowledgments.** Solar wind data was obtained from OMNIweb (http://omniweb.gsfc.nasa.gov/ow_r)
438 Dst index data from the World Data Center for Geomagnetism, Kyoto ([http://wdc.kugi.kyoto-](http://wdc.kugi.kyoto-u.ac.jp/index.html)
439 [u.ac.jp/index.html](http://wdc.kugi.kyoto-u.ac.jp/index.html)) and GOES data from the Nation Oceanic and Atmospheric Admin-
440 istration (<http://www.ngdc.noaa.gov/stp/satellite/goes/dataaccess.html>). This project
441 has received funding from the European Union’s Horizon 2020 research and innovation pro-
442 gramme under grant agreement No 637302 PROGRESS. M. Balikhin and N.Ganushkina
443 thank the International Space Science Institute in Bern, Switzerland, for their support of
444 the international teams on ”Analysis of Cluster Inner Magnetosphere Campaign data, in
445 application the dynamics of waves and wave-particle interaction within the outer radia-
446 tion belt” and ”Ring current modeling: Uncommon Assumptions and Common Miscon-
447 ceptions”.

References

- 448 Baker, D. R., Belian, P., Higbie, R., Klebesadel, and J. Blake, Deep dielectric charging
449 effects due to high-energy electrons in earth’s outer magnetosphere, *Journal of Electro-*
450 *statics*, *20*(1), 3–19, 1987.
- 451 Baker, D. N., R. L. McPherron, T. E. Cayton, and R. W. Klebesadel, Linear prediction
452 filter analysis of relativistic electron properties at 6.6 re, *J. Geophys. Res.*, *95*(A9),
453 15,133–15,140, 1990.

- 454 Balikhin, M. A., O. M. Boaghe, S. A. Billings, and H. S. C. K. Alleyne, Terrestrial
455 magnetosphere as a nonlinear resonator, *Geophys. Res. Lett.*, *28*(6), 11231126, 2001.
- 456 Balikhin, M. A., R. J. Boynton, S. A. Billings, M. Gedalin, N. Ganushkina, D. Coca, and
457 H. Wei, Data based quest for solar wind-magnetosphere coupling function, *Geophys.*
458 *Res. Lett.*, *27*(24), L24,107, 2010.
- 459 Balikhin, M. A., R. J. Boynton, S. N. Walker, J. E. Borovsky, S. A. Billings, and H. L.
460 Wei, Using the narmax approach to model the evolution of energetic electrons fluxes at
461 geostationary orbit, *Geophys. Res. Lett.*, *38*(18), L18,105, 2011.
- 462 Balikhin, M. A., M. Gedalin, G. D. Reeves, R. J. Boynton, and S. A. Billings, Time scaling
463 of the electron flux increase at geo: The local energy diffusion model vs observations,
464 *J. Geophys. Res.*, *117*(A10), A10,208–, 2012.
- 465 Balikhin, M. A., J. V. Rodriguez, R. J. Boynton, S. N. Walker, H. Aryan, D. G. Sibeck,
466 and S. A. Billings, Comparative analysis of noaa refm and snb3geo tools for the forecast
467 of the fluxes of high-energy electrons at geo, *Space Weather*, *14*(1), 2015SW001,303–,
468 2016.
- 469 Beharrell, M. J., and F. Honary, Decoding solar wind-magnetosphere coupling, *Space*
470 *Weather*, *n/a*, 2016SW001,467–, 2016.
- 471 Billings, S., M. Korenberg, and S. Chen, Identification of non-linear output affine systems
472 using an orthogonal least-squares algorithm., *Int. J. of Systems Sci.*, *19*, 1559–1568,
473 1988.
- 474 Billings, S., S. Chen, and M. Korenberg, Identification of mimo non-linear systems using
475 a forward regression orthogonal estimator, *Int. J. Control*, *49*(6), 2157–2189, 1989.

- 476 Billings, S. A., and H. L. Wei, An adaptive orthogonal search algorithm for model subset
477 selection and non-linear system identification, *International Journal of Control*, 81(5),
478 714–724, doi:10.1080/00207170701216311, 2008.
- 479 Blake, J. B., W. A. Kolasinski, R. W. Fillius, and E. G. Mullen, Injection of electrons and
480 protons with energies of tens of mev into l₃ on 24 march 1991, *Geophys. Res. Lett.*,
481 19(8), 821–824, 1992.
- 482 Boaghe, O. M., M. A. Balikhin, S. A. Billings, and H. Alleyne, Identification of nonlinear
483 processes in the magnetospheric dynamics and forecasting of dst index, *J. Geophys.*
484 *Res.*, 106(A12), 30,04730,066, 2001.
- 485 Boynton, R. J., M. A. Balikhin, S. A. Billings, A. S. Sharma, and O. A. Amariutei, Data
486 derived narmax dst model, *Annales Geophysicae*, 29(6), 965–971, doi:10.5194/angeo-
487 29-965-2011_2011a.
- 488 Boynton, R. J., M. A. Balikhin, S. A. Billings, H. L. Wei, and N. Ganushkina, Using the
489 narmax-ols-err algorithm to obtain the most influential coupling functions that affect
490 the evolution of the magnetosphere, *J. Geophys. Res.*, 116(A5), A05,218, 2011b.
- 491 Boynton, R. J., M. A. Balikhin, S. A. Billings, and O. A. Amariutei, Application of
492 nonlinear autoregressive moving average exogenous input models to geospace: advances
493 in understanding and space weather forecasts, *Ann. Geophys.*, 31(9), 1579–1589, 2013a.
- 494 Boynton, R. J., M. A. Balikhin, S. A. Billings, G. D. Reeves, N. Ganushkina, M. Gedalin,
495 O. A. Amariutei, J. E. Borovsky, and S. N. Walker, The analysis of electron fluxes at
496 geosynchronous orbit employing a narmax approach, *J. Geophys. Res. Space Physics*,
497 118(4), 1500–1513, 2013b.

- 498 Boynton, R. J., M. A. Balikhin, and S. A. Billings, Online narmax model for electron
499 fluxes at geo, *Ann. Geophys.*, *33*(3), 405–411, 2015.
- 500 Freeman, J. W., T. P. O'Brien, A. A. Chan, and R. A. Wolf, Energetic electrons at
501 geostationary orbit during the november 3-4, 1993 storm: Spatial/temporal morphology,
502 characterization by a power law spectrum and, representation by an artificial neural
503 network, *J. Geophys. Res.*, *103*(A11), 26,251–26,260, 1998.
- 504 Friedel, R., G. Reeves, and T. Obara, Relativistic electron dynamics in the inner mag-
505 netosphere – a review, *Journal of Atmospheric and Solar-Terrestrial Physics*, *64*(2),
506 265–282, 2002.
- 507 Friederich, U., D. Coca, S. A. Billings, and M. Juusola, Data modelling for analysis of
508 adaptive changes in fly photoreceptors, *NEURAL INFORMATION PROCESSING, PT*
509 *1, PROCEEDINGS*, *5863*, 34–38, 2009.
- 510 Ganushkina, N. Y., O. A. Amariutei, Y. Y. Shprits, and M. W. Liemohn, Transport of the
511 plasma sheet electrons to the geostationary distances, *J. Geophys. Res. Space Physics*,
512 *118*(1), 82–98, 2013.
- 513 Ganushkina, N. Y., M. W. Liemohn, O. A. Amariutei, and D. Pitchford, Low-energy
514 electrons (5–50 keV) in the inner magnetosphere, *J. Geophys. Res. Space Physics*, *119*(1),
515 246–259, 2014.
- 516 Ganushkina, N. Y., O. A. Amariutei, D. Welling, and D. Heynderickx, Nowcast
517 model for low-energy electrons in the inner magnetosphere, *Space Weather*, *13*(1),
518 2014SW001,098–, 2015.
- 519 Gubby, R., and J. Evans, Space environment effects and satellite design, *Journal of At-*
520 *mospheric and Solar-Terrestrial Physics*, *64*(16), 1723–1733, 2002.

- 521 Guo, Y., L. Guo, S. Billings, and H.-L. Wei, An iterative orthogonal forward re-
522 gression algorithm, *International Journal of Systems Science*, *46*(5), 776–789, doi:
523 10.1080/00207721.2014.981237, 2014.
- 524 Hanser, F. A., Eps/hepad calibration and data handbook, *Tech. rep.*, Tech. Rep. GOESN-
525 ENG-048D, Assurance Technol. Corp., Carlisle, Mass., 2011.
- 526 Horne, R. B., S. A. Glauert, N. P. Meredith, D. Boscher, V. Maget, D. Heynderickx, and
527 D. Pitchford, Space weather impacts on satellites and forecasting the earth’s electron
528 radiation belts with spacecast, *Space Weather*, *11*, 1–18, 2013a.
- 529 Horne, R. B., S. A. Glauert, N. P. Meredith, H. Koskinen, R. Vainio, A. Afanasiev,
530 N. Y. Ganushkina, O. A. Amariutei, D. Boscher, A. Sicard, V. Maget, S. Poedts,
531 C. Jacobs, B. Sanahuja, A. Aran, D. Heynderickx, and D. Pitchford, Forecasting the
532 earth’s radiation belts and modelling solar energetic particle events: Recent results from
533 spacecast, *J. Space Weather Space Clim.*, *3*, A20, 2013b.
- 534 Koons, H. C., and D. J. Gorney, A neural network model of the relativistic electron flux
535 at geosynchronous orbit, *J. Geophys. Res.*, *96*(A4), 5549–5556, 1991.
- 536 Leontaritis, I. J., and S. A. Billings, Input-output parametric models for non-linear sys-
537 tems part I: Deterministic non-linear systems., *Int. J. Control*, *41* (2), 303–328, 1985a.
- 538 Leontaritis, I. J., and S. A. Billings, Input-output parametric models for non-linear sys-
539 tems part II: Stochastic nonlinear systems, *Int. J. Control*, *41* (2), 329–344, 1985b.
- 540 Li, W., B. Ni, R. M. Thorne, J. Bortnik, J. C. Green, C. A. Kletzing, W. S. Kurth, and
541 G. B. Hospodarsky, Constructing the global distribution of chorus wave intensity using
542 measurements of electrons by the poes satellites and waves by the van allen probes,
543 *Geophys. Res. Lett.*, *40*(17), 4526–4532, 2013.

- 544 Li, X., Variations of 0.7-6.0 mev electrons at geosynchronous orbit as a function of solar
545 wind, *Space Weather*, 2(3), S03,006, 2004.
- 546 Ling, A. G., G. P. Ginet, R. V. Hilmer, and K. L. Perry, A neural network-based geosyn-
547 chronous relativistic electron flux forecasting model, *Space Weather*, 8(9), S09,003–,
548 2010.
- 549 Lohmeyer, W., and K. Cahoy, Space weather radiation effects on geostationary satellite
550 solid-state power amplifiers, *Space Weather*, 11(8), 476–488, 2013.
- 551 Lohmeyer, W., A. Carlton, F. Wong, M. Bodeau, A. Kennedy, and K. Cahoy, Response
552 of geostationary communications satellite solid-state power amplifiers to high-energy
553 electron fluence, *Space Weather*, 13(5), 2014SW001,147–, 2015.
- 554 Mao, K. Z., and S. A. Billings, Algorithms for minimal model structure detection in
555 nonlinear dynamic system identification, *International Journal of Control*, 68(2), 311–
556 330, doi:10.1080/002071797223631, 1997.
- 557 Mourenas, D., A. V. Artemyev, O. V. Agapitov, V. Krasnoselskikh, and W. Li, Approxi-
558 mate analytical solutions for the trapped electron distribution due to quasi-linear diffu-
559 sion by whistler mode waves, *J. Geophys. Res. Space Physics*, 119(12), 2014JA020,443–,
560 2014.
- 561 Mullen, E. G., M. S. Gussenhoven, D. A. Hardy, T. A. Aggson, B. G. Ledley, and
562 E. Whipple, Scatha survey of high-level spacecraft charging in sunlight, *J. Geophys.*
563 *Res.*, 91(A2), 1474–1490, 1986.
- 564 Olsen, R. C., A threshold effect for spacecraft charging, *J. Geophys. Res.*, 88(A1), 493–
565 499, 1983.

- 566 Osthus, D., P. C. Caragea, D. Higdon, S. K. Morley, G. D. Reeves, and B. P. Weaver,
567 Dynamic linear models for forecasting of radiation belt electrons and limitations on
568 physical interpretation of predictive models, *Space Weather*, *12*(6), 426–446, 2014.
- 569 Rastatter, L., M. M. Kuznetsova, A. Glocer, D. Welling, X. Meng, J. Raeder, M. Wilt-
570 berger, V. I. Jordanova, Y. Yu, S. Zaharia, R. S. Weigel, S. Sazykin, R. Boynton,
571 H. Wei, V. Eccles, W. Horton, M. L. Mays, and J. Gannon, Geospace environment
572 modeling 2008-2009 challenge: Dst index, *Space Weather*, *11*(4), 187–205, 2013.
- 573 Reeves, G. D., Relativistic electrons and magnetic storms: 1992-1995, *Geophys. Res. Lett.*,
574 *25*(11), 1817–1820, 1998.
- 575 Temerin, M., and X. Li, Dst model for 1995 - 2002, *J. Geophys. Res.*, *111*(A4), A04,221,
576 2006.
- 577 Wei, H. L., and S. A. Billings, An efficient nonlinear cardinal b-spline model for high
578 tide forecasts at the venice lagoon, *Nonlinear Processes In Geophysics*, *13*(5), 577–584,
579 2006.
- 580 Wei, H. L., and S. A. Billings, Model structure selection using an integrated forward
581 orthogonal search algorithm assisted by squared correlation and mutual information,
582 *Int. J. Modelling, Identification and Control*, *3*, 341–356, 2008.
- 583 Wei, H. L., S. A. Billings, and M. Balikhin, Prediction of the dst index using multireso-
584 lution wavelet models, *J. Geophys. Res.*, *109*(A7), A07,212, 2004.
- 585 Wei, H.-L., S. A. Billings, A. Surjalal Sharma, S. Wing, R. J. Boynton, and S. N. Walker,
586 Forecasting relativistic electron flux using dynamic multiple regression models, *Annales*
587 *Geophysicae*, *29*(2), 415–420, doi:10.5194/angeo-29-415-2011, 2011.

Table 1. Table showing the performance of the five low energy electron flux models as well as the Forecast length

Model	Forecast Horizon	1-day PE (%)	1-day CC (%)	1-hour PE (%)	1-hour CC (%)
30-50 keV	10 hr	72.0	84.9	66.9	82.0
50-100 keV	12 hr	70.7	84.2	69.2	83.5
100-200 keV	16 hr	71.1	84.4	73.2	85.6
200-350 keV	24 hr	69.5	83.7	71.6	84.9
350-600 keV	24 hr	69.9	83.8	73.6	85.9

Figure 1. Panel (a) shows the past 24 hour average > 800 keV electron flux measured by GOES in blue and the model 24 hour ahead forecast in orange for the period from 1 January 2011 to 28 February 2015, while panel (b) shows the > 800 keV electron flux model error ($\log_{10}(J_{GOES}) - \log_{10}(J_{model})$). Panel (c) shows the past 24 hour average > 2 MeV electron flux measured by GOES in blue and the model 24 hour ahead forecast in orange for the period from 1 January 2011 to 28 February 2015, while panel (b) shows the > 2 MeV electron flux model error ($\log_{10}(J_{GOES}) - \log_{10}(J_{model})$).

Figure 2. (a) The 30-50 keV electron flux for the 9 telescopes. (b) The pitch angle of each telescope. For the period from 13 November 2012 to 27 February 2013

Figure 3. The PE of a 30-50 keV model between 1 May 2010 and 28 February 2011 vs the minimum log included in that model.

Figure 4. The daily average 30-50 keV (a), 50-100 keV (c) and 100-200 keV (e) electron flux measured by GOES in blue and the model forecast in orange for the period from 1 March 2013 to 28 February 2015, and 30-50 keV (b), 50-100 keV (d) and 100-200 keV (f) model error ($\log_{10}(J_{GOES}) - \log_{10}(J_{model})$).

588 Wrenn, G. L., D. J. Rodgers, and K. A. Ryden, A solar cycle of spacecraft anomalies due
589 to internal charging, *Ann. Geophys.*, *20*(7), 953–956, 2002.

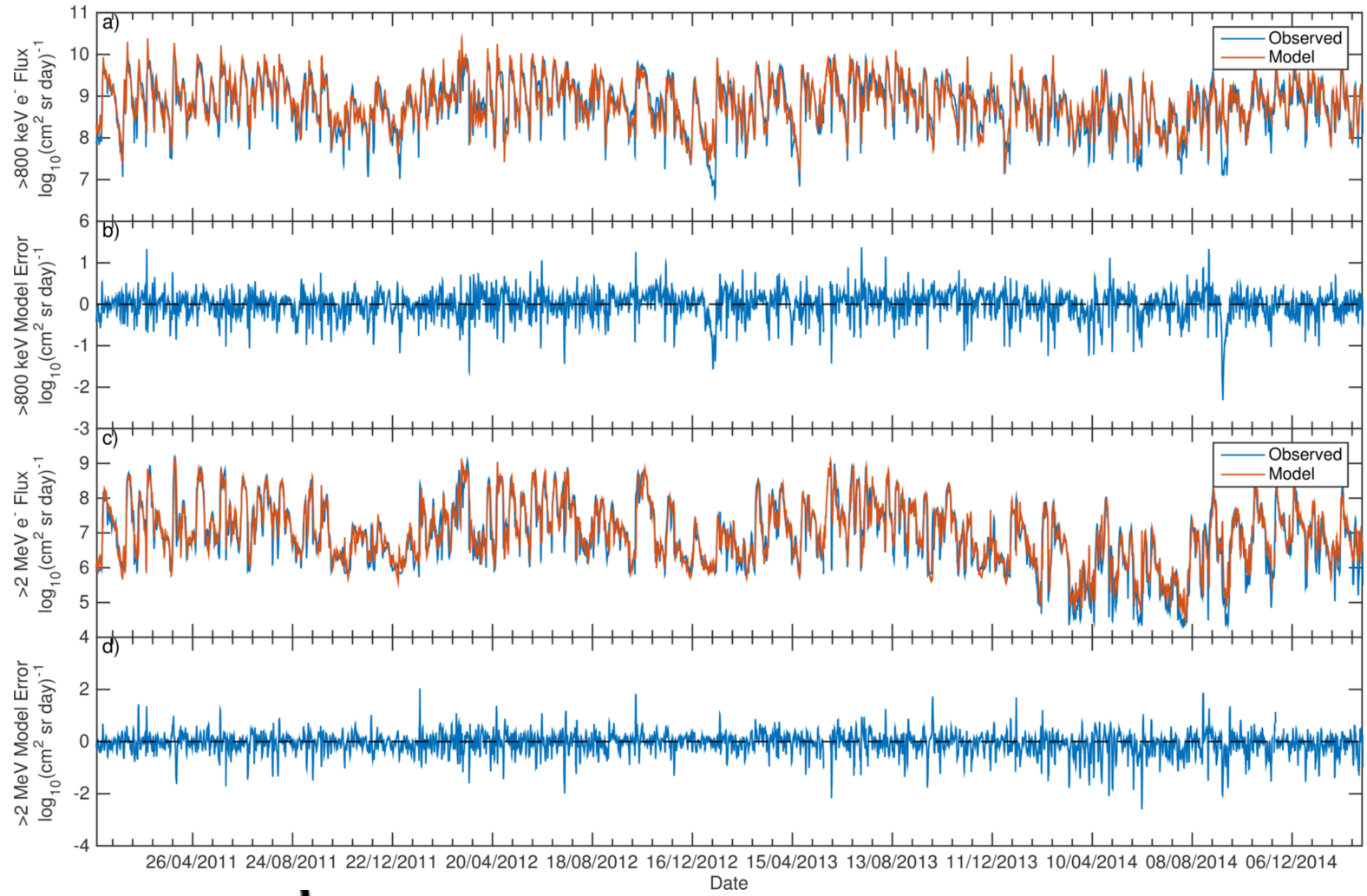
Figure 5. The daily average 200-350 keV (a) and 350-600 keV (c) electron flux measured by GOES in blue and the model 24 hour ahead forecast in orange for the period from 1 March 2013 to 28 February 2015, and 200-350 keV (b) and 350-600 keV (d) model error ($\log_{10}(J_{GOES}) - \log_{10}(J_{model})$).

Figure 6. Distribution of the model errors ($\log_{10}(J_{GOES}) - \log_{10}(J_{model})$) for the MAGED energy channels with the variance of the model errors, σ_e , shown in the top right of each panel (Panels (a), (c), (e), (g), (i)). Distribution of the model errors when $Dst < -40$ nT (Panels (b), (d), (f), (h), (j)).

Figure 7. Distribution of the model errors ($\log_{10}(J_{GOES}) - \log_{10}(J_{model})$) for the EPS energy channels with the variance of the model errors, σ_e , shown in the top right of each panel (Panels (a), (c)). Distribution of the model errors when $Dst < -40$ nT (Panels (b), (d)).

Figure 8. The daily average electron flux measured by GOES in blue and the model forecast in orange for the period from 15 April 2013 to 15 May 2013 (Panel (a) 30-50 keV; (b) 50-100 keV; (c) 100-200 keV; (d) 200-350 keV; (e) 350-600 keV; (f) >800 keV; (g) >2 MeV), with the Dst index in Panel (h).

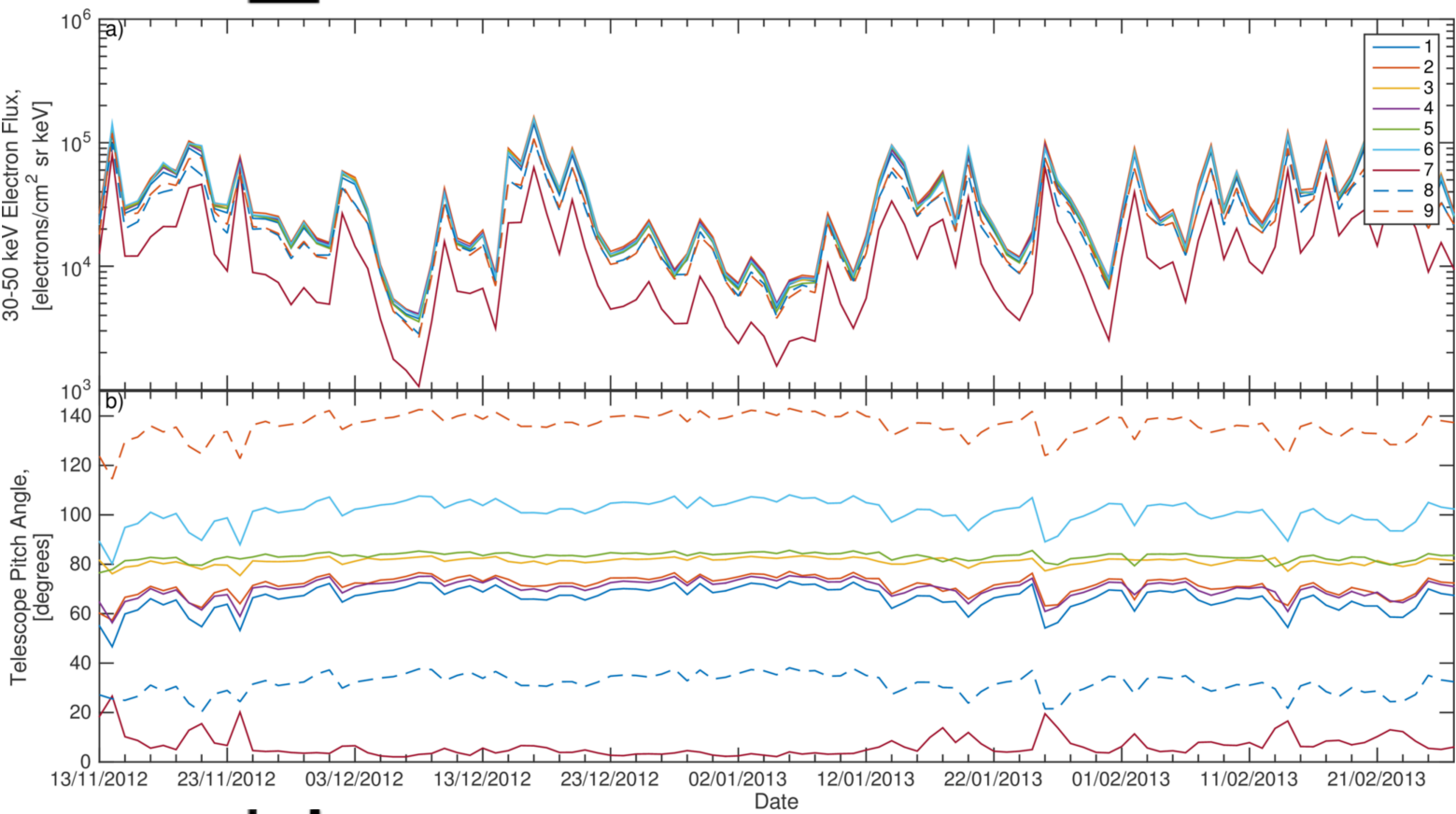
pt



Al

2016sw001506-f01-z-eps

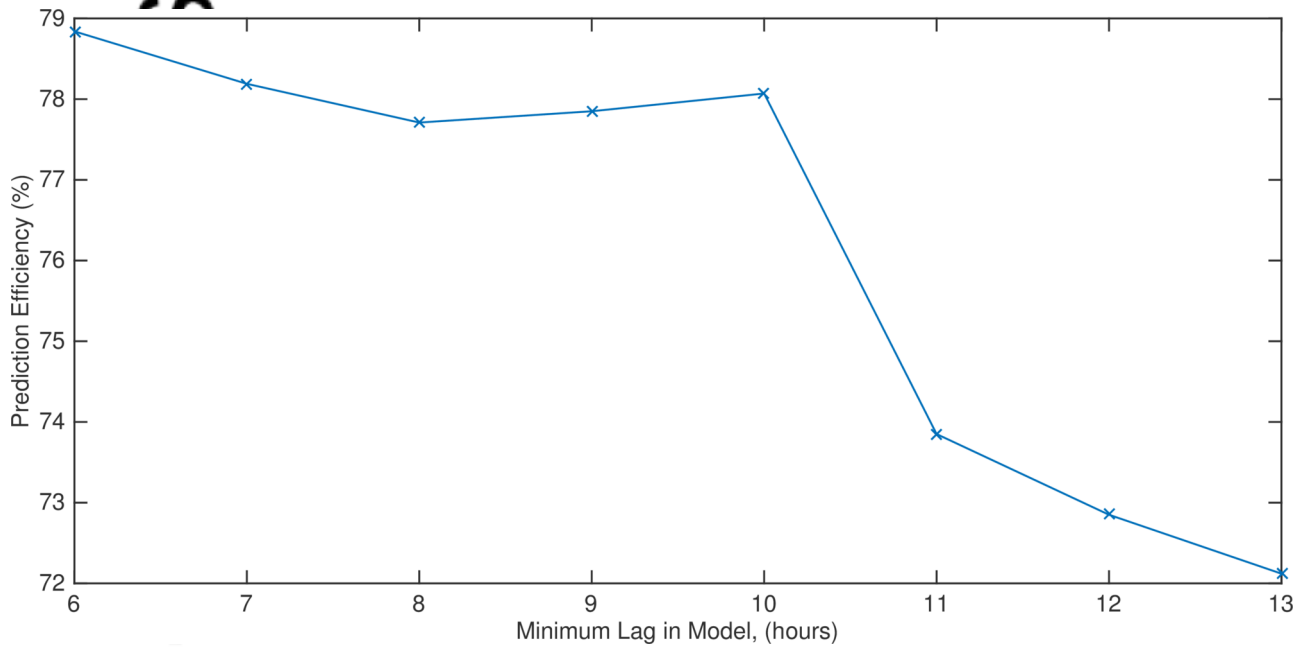
ript



2016sw001506-f02-z-eps

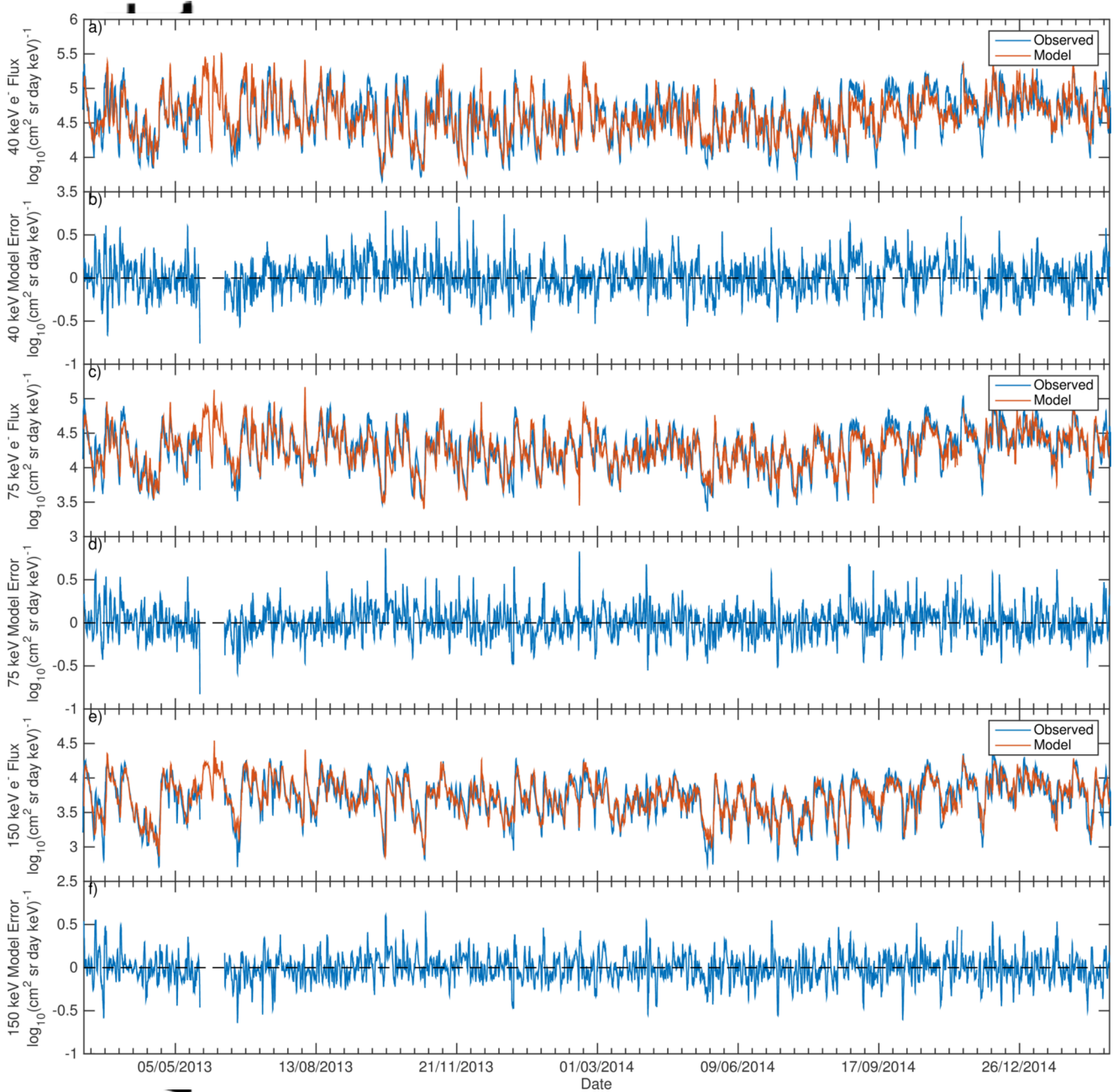
Aut

script



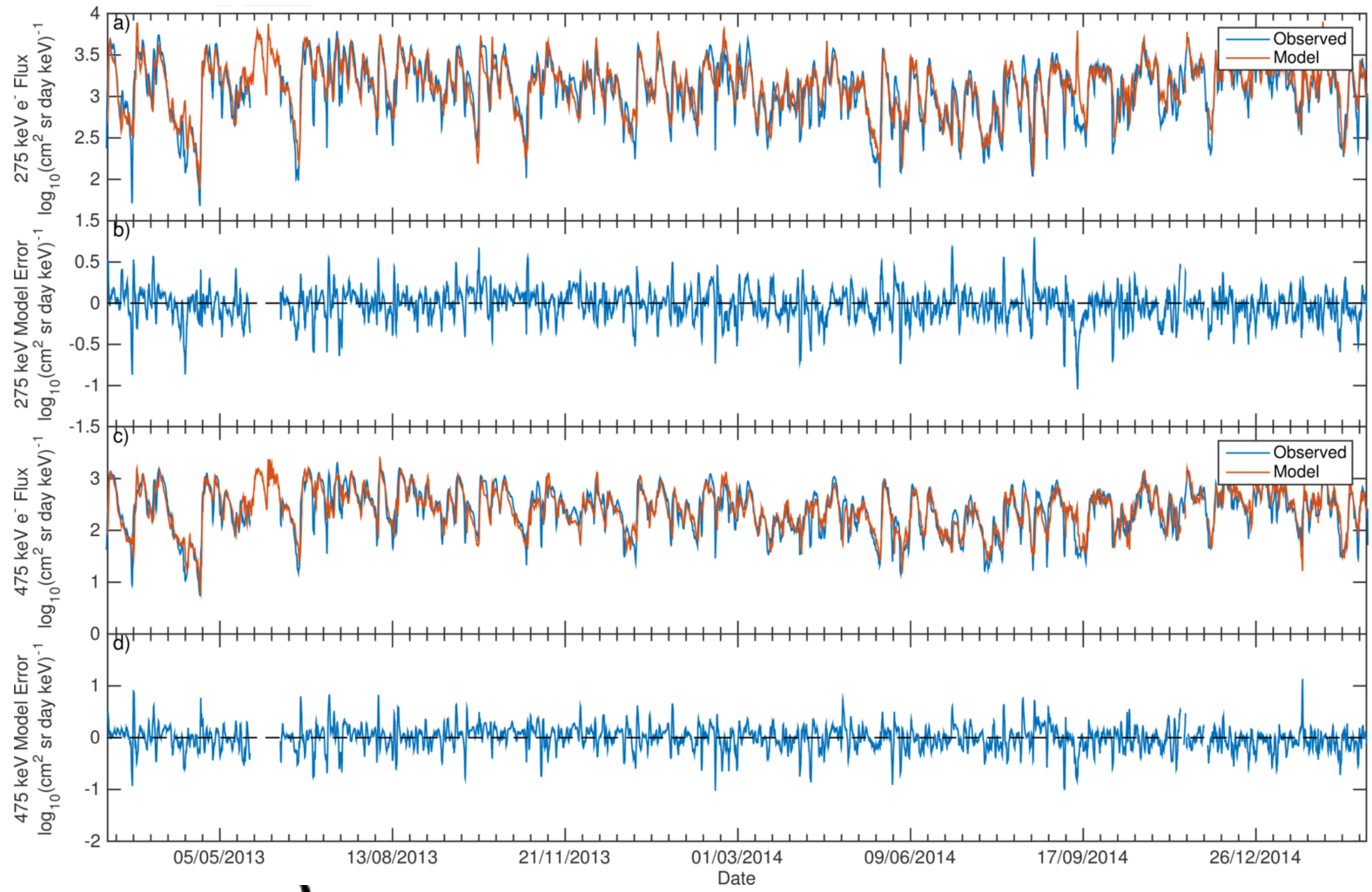
Auth

2016sw001506-f03-z-eps



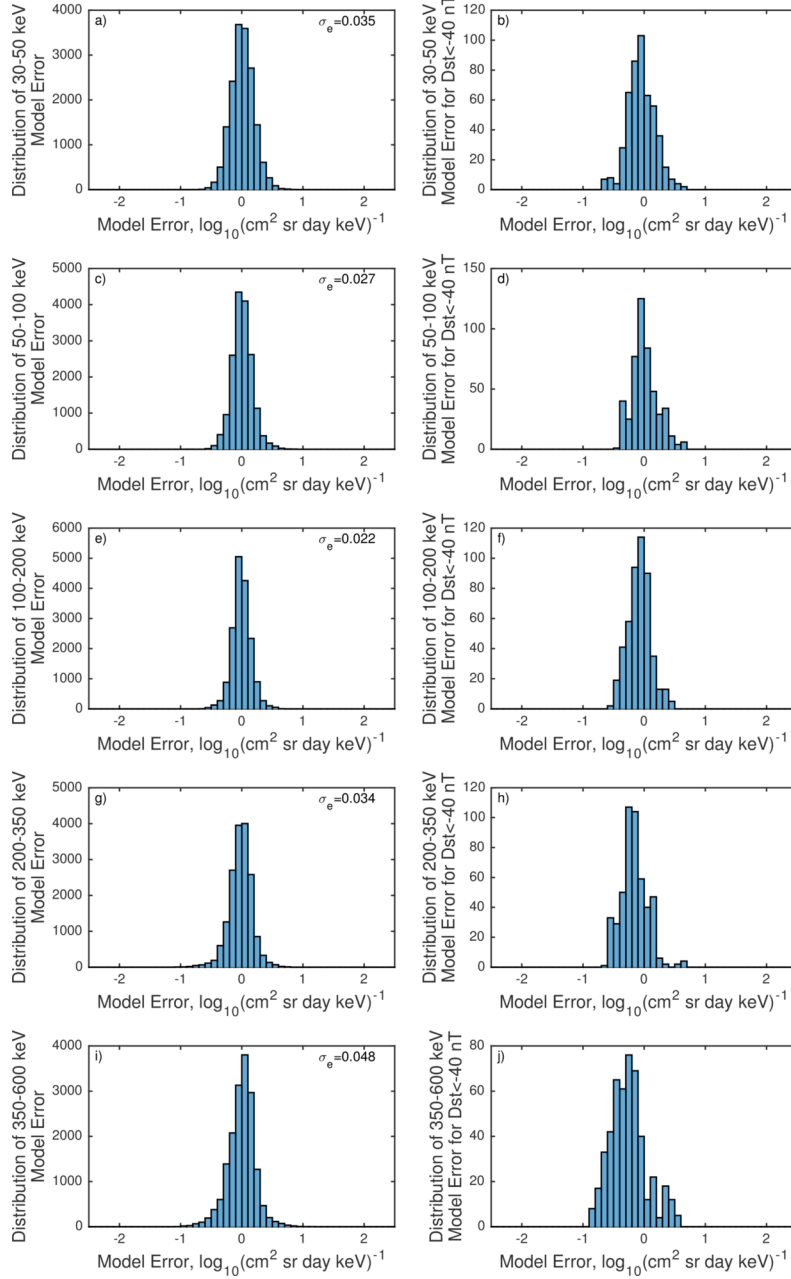
2016sw001506-f04-z.eps

pt



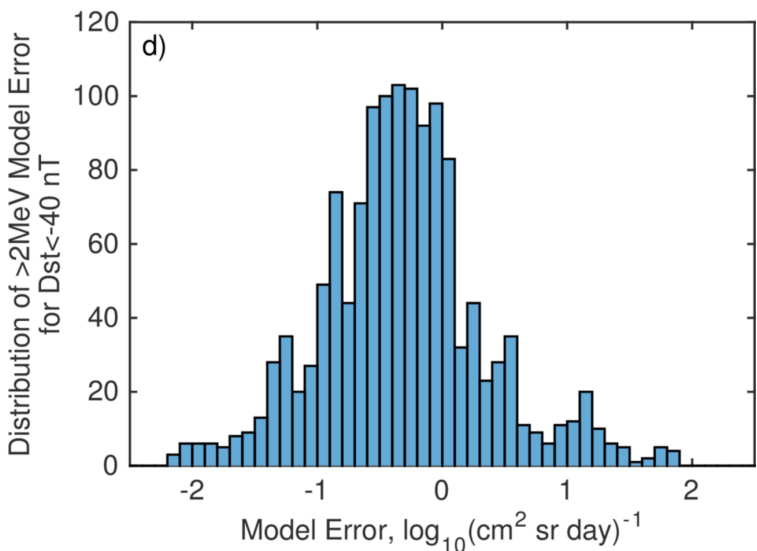
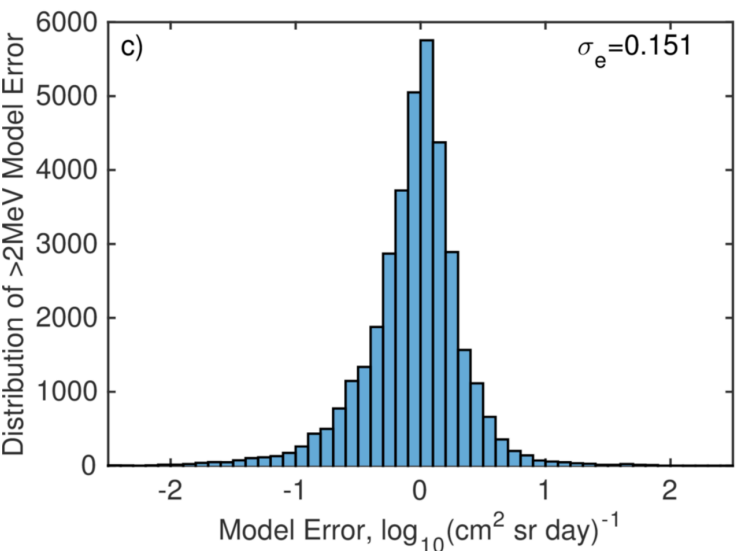
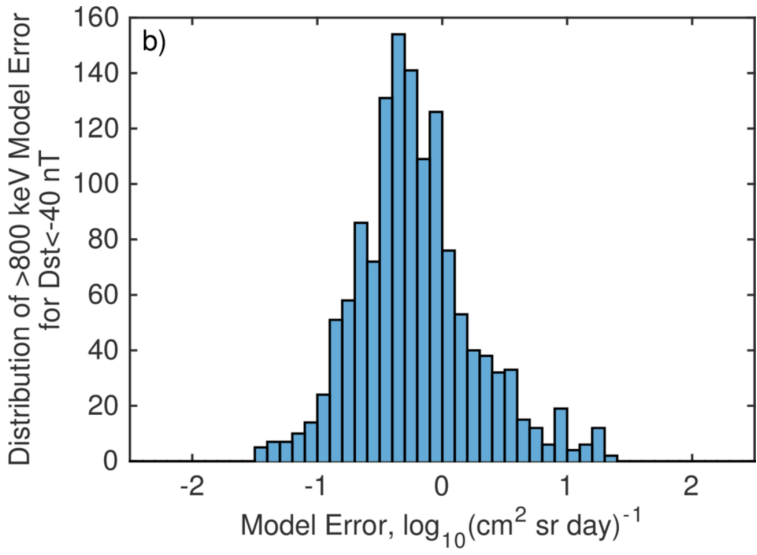
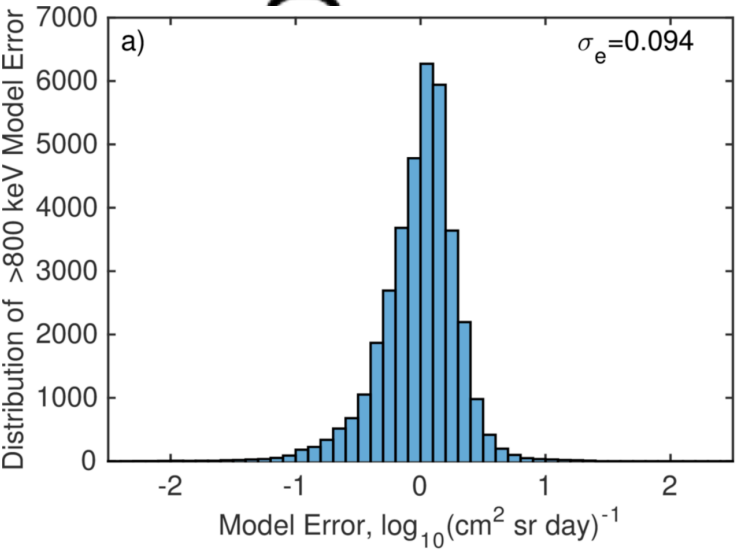
2016sw001506-f05-z-eps

Al



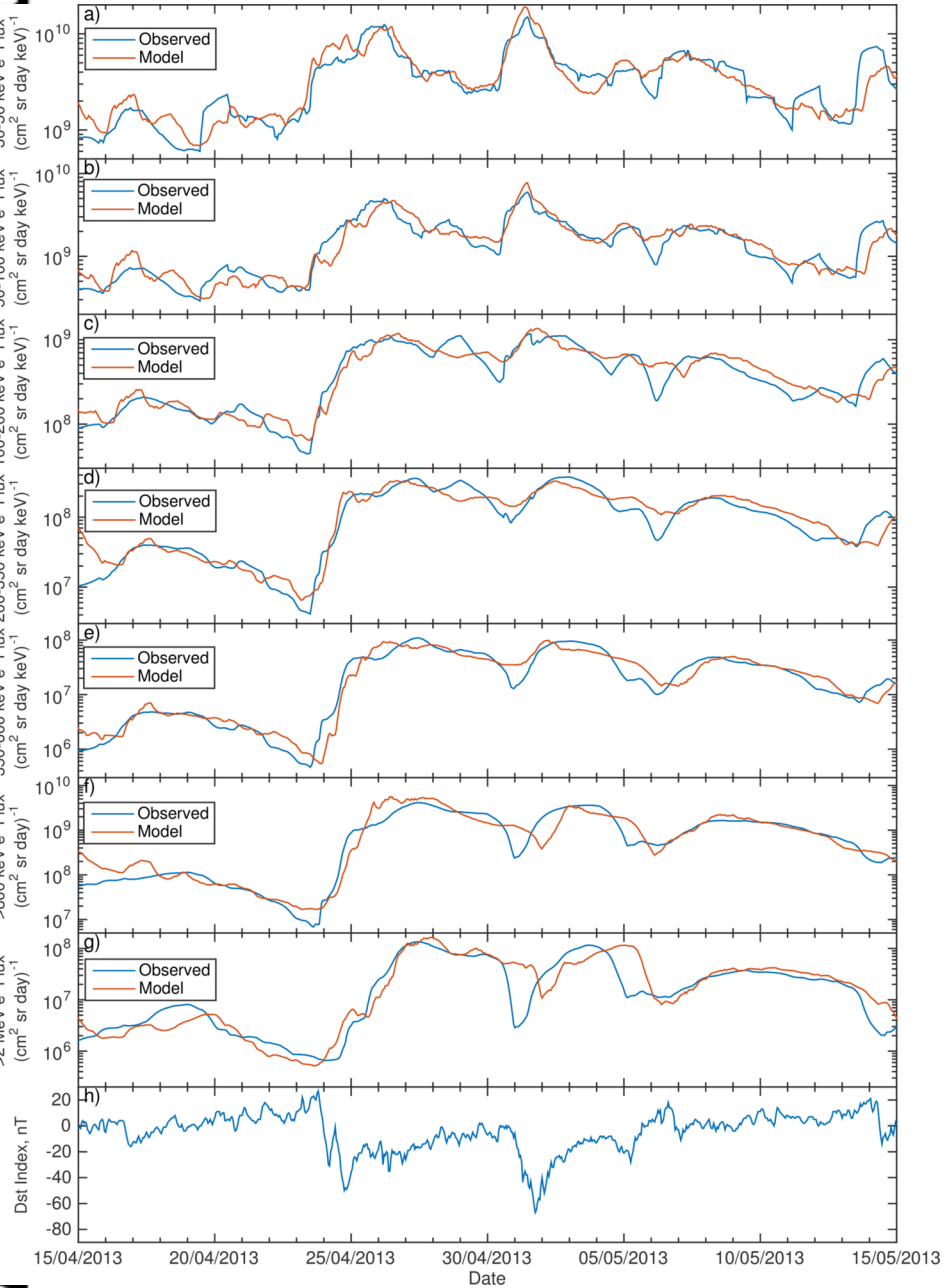
2016sw001506-f06-z.eps

t



A

2016sw001506-f07-z-eps



2016sw001506-f08-z.eps